



# UNCOVER: A NIRSpec Identification of a Broad-line AGN at $z = 8.50$

Vasily Kokorev<sup>1</sup>, Seiji Fujimoto<sup>2,3</sup>, Ivo Labbe<sup>4</sup>, Jenny E. Greene<sup>5</sup>, Rachel Bezanson<sup>6</sup>, Pratika Dayal<sup>1</sup>, Erica J. Nelson<sup>7</sup>, Hakim Atek<sup>8</sup>, Gabriel Brammer<sup>3</sup>, Karina I. Caputi<sup>1,3</sup>, Iryna Chemerynska<sup>8</sup>, Sam E. Cutler<sup>9</sup>, Robert Feldmann<sup>10</sup>, Yoshinobu Fudamoto<sup>11,12</sup>, Lukas J. Furtak<sup>13</sup>, Andy D. Goulding<sup>5</sup>, Anna de Graaff<sup>14</sup>, Joel Leja<sup>15,16,17</sup>, Danilo Marchesini<sup>18</sup>, Tim B. Miller<sup>19,20</sup>, Themiya Nanayakkara<sup>4</sup>, Pascal A. Oesch<sup>3,21</sup>, Richard Pan<sup>18</sup>, Sedona H. Price<sup>6</sup>, David J. Setton<sup>6</sup>, Renske Smit<sup>22</sup>, Mauro Stefanon<sup>23,24</sup>, Bingjie Wang (王冰洁)<sup>15,16,17</sup>, John R. Weaver<sup>9</sup>, Katherine E. Whitaker<sup>3,9</sup>, Christina C. Williams<sup>25,26</sup>, and Adi Zitrin<sup>13</sup>

<sup>1</sup> Kapteyn Astronomical Institute, University of Groningen, 9700 AV Groningen, The Netherlands; [kokorev@astro.rug.nl](mailto:kokorev@astro.rug.nl)

<sup>2</sup> Department of Astronomy, The University of Texas at Austin, Austin, TX 78712, USA

<sup>3</sup> Cosmic Dawn Center (DAWN), Niels Bohr Institute, University of Copenhagen, Jagtvej 128, København N, DK-2200, Denmark

<sup>4</sup> Centre for Astrophysics and Supercomputing, Swinburne University of Technology, Melbourne, VIC 3122, Australia

<sup>5</sup> Department of Astrophysical Sciences, Princeton University, 4 Ivy Lane, Princeton, NJ 08544, USA

<sup>6</sup> Department of Physics and Astronomy and PITT PACC, University of Pittsburgh, Pittsburgh, PA 15260, USA

<sup>7</sup> Department of Astrophysical and Planetary Science, University of Colorado, Boulder, CO 80309, USA

<sup>8</sup> Institut d'Astrophysique de Paris, CNRS, Sorbonne Université, 98bis Boulevard Arago, F-75014, Paris, France

<sup>9</sup> Department of Astronomy, University of Massachusetts, Amherst, MA 01003, USA

<sup>10</sup> Institute for Computational Science, University of Zurich, Zurich, CH-8057, Switzerland

<sup>11</sup> Waseda Research Institute for Science and Engineering, Faculty of Science and Engineering, Waseda University, 3-4-1 Okubo, Shinjuku, Tokyo 169-8555, Japan

<sup>12</sup> National Astronomical Observatory of Japan, 2-21-1, Osawa, Mitaka, Tokyo, Japan

<sup>13</sup> Physics Department, Ben-Gurion University of the Negev, P.O. Box 653, Be'er-Sheva 84105, Israel

<sup>14</sup> Max-Planck-Institut für Astronomie, Königstuhl 17, D-69117, Heidelberg, Germany

<sup>15</sup> Department of Astronomy & Astrophysics, The Pennsylvania State University, University Park, PA 16802, USA

<sup>16</sup> Institute for Computational & Data Sciences, The Pennsylvania State University, University Park, PA 16802, USA

<sup>17</sup> Institute for Gravitation and the Cosmos, The Pennsylvania State University, University Park, PA 16802, USA

<sup>18</sup> Department of Physics & Astronomy, Tufts University, Medford, MA 02155, USA

<sup>19</sup> Department of Astronomy, Yale University, New Haven, CT 06511, USA

<sup>20</sup> Center for Interdisciplinary Exploration and Research in Astrophysics (CIERA) and Department of Physics and Astronomy, Northwestern University, 1800 Sherman Avenue, Evanston, IL 60201, USA

<sup>21</sup> Department of Astronomy, University of Geneva, Chemin Pegasi 51, 1290 Versoix, Switzerland

<sup>22</sup> Astrophysics Research Institute, Liverpool John Moores University, 146 Brownlow Hill, Liverpool L3 5RF, UK

<sup>23</sup> Departament d'Astronomia i Astrofísica, Universitat de València, C. Dr. Moliner 50, E-46100 Burjassot, València, Spain

<sup>24</sup> Unidad Asociada CSIC "Grupo de Astrofísica Extragaláctica y Cosmología" (Instituto de Física de Cantabria—Universitat de València), Spain

<sup>25</sup> NSF's National Optical-Infrared Astronomy Research Laboratory, 950 North Cherry Avenue, Tucson, AZ 85719, USA

<sup>26</sup> Steward Observatory, University of Arizona, 933 North Cherry Avenue, Tucson, AZ 85721, USA

Received 2023 August 24; revised 2023 October 4; accepted 2023 October 15; published 2023 October 26

## Abstract

Deep observations with the James Webb Space Telescope (JWST) have revealed an emerging population of red pointlike sources that could provide a link between the postulated supermassive black hole seeds and observed quasars. In this work, we present a JWST/NIRSpec spectrum from the JWST Cycle 1 UNCOVER Treasury survey of a massive accreting black hole at  $z = 8.50$  displaying a clear broad-line component as inferred from the  $H\beta$  line with  $\text{FWHM} = 3439 \pm 413 \text{ km s}^{-1}$ , typical of the broad-line region of an active galactic nucleus (AGN). The AGN nature of this object is further supported by high ionization, as inferred from emission lines, and a point-source morphology. We compute a black hole mass of  $\log_{10}(M_{\text{BH}}/M_{\odot}) = 8.17 \pm 0.42$  and a bolometric luminosity of  $L_{\text{bol}} \sim 6.6 \times 10^{45} \text{ erg s}^{-1}$ . These values imply that our object is accreting at  $\sim 40\%$  of the Eddington limit. Detailed modeling of the spectral energy distribution in the optical and near-infrared, together with constraints from ALMA, indicate an upper limit on the stellar mass of  $\log_{10}(M_{*}/M_{\odot}) < 8.7$ , which would lead to an unprecedented ratio of black hole to host mass of at least  $\sim 30\%$ . This is orders of magnitude higher compared to the local QSOs but consistent with recent AGN studies at high redshift with JWST. This finding suggests that a nonnegligible fraction of supermassive black holes either started out from massive seeds and/or grew at a super-Eddington rate at high redshift. Given the predicted number densities of high- $z$  faint AGN, future NIRSpec observations of larger samples will allow us to further investigate galaxy–black hole coevolution in the early Universe.

*Unified Astronomy Thesaurus concepts:* Active galactic nuclei (16); High-redshift galaxies (734); Early universe (435)



Original content from this work may be used under the terms of the [Creative Commons Attribution 4.0 licence](https://creativecommons.org/licenses/by/4.0/). Any further distribution of this work must maintain attribution to the author(s) and the title of the work, journal citation and DOI.

## 1. Introduction

Over the past few decades, observations have established a sample of more than 200 bright active galactic nuclei (AGN) at  $z > 6$  powered by accretion onto massive black holes (BHs; e.g., Fan et al. 2001; Kashikawa et al. 2015; Matsuoka et al. 2018). Lying well within the first billion years, many of these BHs are massive ( $\sim 10^{8-10} M_{\odot}$ ; Bañados et al. 2018; Inayoshi et al. 2020), with the heaviest BH having a mass of about  $1.6 \times 10^9$  only 700 million yr after the Big Bang (Wang et al. 2021). The presence of such supermassive black holes (SMBHs) is extremely hard to reconcile with BH formation and growth scenarios, since they require extremely massive seeds (of  $\sim 1300 M_{\odot}$ ) to form shortly after the Big Bang and then continuously and rapidly accrete gas at the Eddington rate (the physical limit at which outward radiation pressure balances inward gravitational force). One possible solution to explain the presence of such SMBHs lies in invoking super-Eddington accretion rates (e.g., Haiman & Loeb 2001; Alexander & Natarajan 2014) to drive the growth of low-mass BH seeds ( $\sim 100 M_{\odot}$ ) formed from the first (metal-free Population III) stars (Madau & Rees 2001). Another possible solution is to start from massive seeds that include “nuclear clusters” of  $10^{2-4} M_{\odot}$  from the collapse or coalescence of massive stars in compact stellar clusters (Omukai et al. 2008; Schleicher et al. 2022) or even heavier “direct-collapse black hole” (DCBH) seeds of  $> 10^3 M_{\odot}$  from the collapse of pristine gas in early halos (Rees 1984; Loeb & Rasio 1994).

Observations with the James Webb Space Telescope (JWST) have started to discover previously missing UV-faint AGN. These have been identified through a combination of broad and high-ionization lines (Furtak et al. 2023a; Goulding et al. 2023; Harikane et al. 2023; Kocevski et al. 2023; Larson et al. 2023; Maiolino et al. 2023a, 2023b; Übler et al. 2023) or from color and morphology (Barro et al. 2023; Matthee et al. 2023; Yang et al. 2023). In common across these selections are extremely red rest-frame optical colors, a flat  $f_{\lambda}$  UV continuum, and a generally very compact morphology. When spectra are available, broad Balmer series lines, such as  $H\alpha$  or  $H\beta$ , are a telltale sign of ongoing accretion. While these are UV-faint, they span a large range of bolometric luminosities,  $L_{\text{bol}} \sim 10^{43} - 10^{46}$  erg s $^{-1}$ , and BH masses,  $M_{\text{BH}} \sim 10^6 - 10^8 M_{\odot}$ , with some of them being strongly dust-obscured, up to  $A_V \sim 3$  (Furtak et al. 2023a). In addition, Labbé et al. (2023a, 2023b) recently presented a large photometrically selected sample of AGN in the UNCOVER Cycle I JWST program. These have been modeled with a composite spectral energy distribution (SED) model, which consists of a dust-reddened type I AGN plus an additional UV component attributed to either the scattered light or star formation. The unique findings present across all of these works are the high number densities of reddened QSOs, suggesting that a nonnegligible fraction of BH growth at these epochs is taking place behind a thick veil of dust.

In this work, we report a secure detection of the broad-line (BL) AGN emission at  $z = 8.50$ . The point source hosting the AGN was first identified as one of the “little red dots” (Greene et al. 2023; Labbé et al. 2023a) in the UNCOVER NIRCcam sample. Here we report the results from JWST/NIRSpec Micro-Shutter Assembly (MSA) observations of this source in the UNCOVER field (PIs: I. Labbé, R. Bezanson; Bezanson et al. 2022). The exquisite high signal-to-noise ratio (S/N) NIRSpec spectrum allows us to resolve a multitude of lines, including  $H\beta$  and [O III]  $\lambda\lambda 4959, 5007$ , and clearly

demonstrate the presence of the BL emission in  $H\beta$ . The [O III]  $\lambda\lambda 4959, 5007$  lines, however, only display narrow emission, which, in conjunction with a nearly pointlike morphology and the presence of highly ionized gas, provide strong evidence for AGN activity in our source. Clear BL emission in  $H\beta$  would make our source the highest-redshift BL AGN with a secure (S/N  $> 10$ ) Balmer BL identification to date (see also Larson et al. 2023).

Throughout this work, we assume a flat  $\Lambda$ CDM cosmology with  $\Omega_{\text{m},0} = 0.3$ ,  $\Omega_{\Lambda,0} = 0.7$ , and  $H_0 = 70$  km s $^{-1}$  Mpc $^{-1}$  and a Chabrier (2003) initial mass function between 0.1 and  $100 M_{\odot}$ . All magnitudes are expressed in the AB system (Oke 1974).

## 2. Observations and Data

### 2.1. NIRSpec Setup

Initially identified as a potential high- $z$  AGN candidate via broad- and medium-band NIRCcam photometry (Labbé et al. 2023a, 2023b; Weaver et al. 2023), UNCOVER ID 20466<sup>27</sup> is located at R.A. = 3 $^{\circ}$ :640408, decl. =  $-30^{\circ}$ :386438. The target was observed for a total of 2.7 hr with the low-resolution PRISM on 2023 July 31 as a part of the MSA follow-up program of the UNCOVER JWST field A2744 (Bezanson et al. 2022). These observations employed a 2-POINT-WITH-NIRCcam-SIZE2 dither pattern and a three-shutter slitlet nod pattern at an aperture angle of  $\sim 44^{\circ}$ . We show the positions of these slits overlaid on a  $2''$  cutout of our source in Figure 1. For further details of the observational setup, see Bezanson et al. (2022) and S. Price et al. (2023, in preparation).

### 2.2. PRISM Data Reduction and Calibration

The UNCOVER MSA spectra were reduced using MSAEXP (v0.6.10; Brammer 2022), starting from the level 2 data products obtained from MAST.<sup>28</sup> The pipeline applies corrections to the  $1/f$  noise, identifies artifacts (e.g., “snowballs”) in the calibrated files, and removes bias in individual exposures by computing a simple median (e.g., see Rigby et al. 2023). Additional parts of the JWST reduction pipeline are used to set the slit WCS, perform slit-level flat-fielding, and compute the path-loss corrections. Each of the 2D slits are then extracted and drizzled onto a common pixel grid. The local background subtraction is performed by using the shifted, stacked 2D spectra. To obtain the final 1D spectrum, MSAEXP performs an adaptive optimal extraction of the background-subtracted 2D trace by fitting a Gaussian model where the center and width are allowed to vary (e.g., Horne 1986); a similar procedure was used in Goulding et al. (2023) and Wang et al. (2023).

It is important to note that the absolute normalization of the spectrum can be affected by many factors, which include but are not necessarily limited to path-loss correction, calibration uncertainty,<sup>29</sup> astrometric slit position uncertainty, location and extent of the source within a slitlet, and source self-subtraction when correcting for the local background effects. To account for these potential calibration issues and determine a total slit-loss correction, we perform an additional flux rescaling by convolving the extracted 1D spectrum with all of the broad-/medium-band NIRCcam filters and compare our flux densities to

<sup>27</sup> Corresponds to the MSA ID taken from internal UNCOVER catalog v2.2.1.

<sup>28</sup> Available from <https://doi.org/10.17909/8k5c-xr27>.

<sup>29</sup> Can be of the order of 10%–20%; <https://jwst-docs.stsci.edu/jwst-near-infrared-spectrograph>.

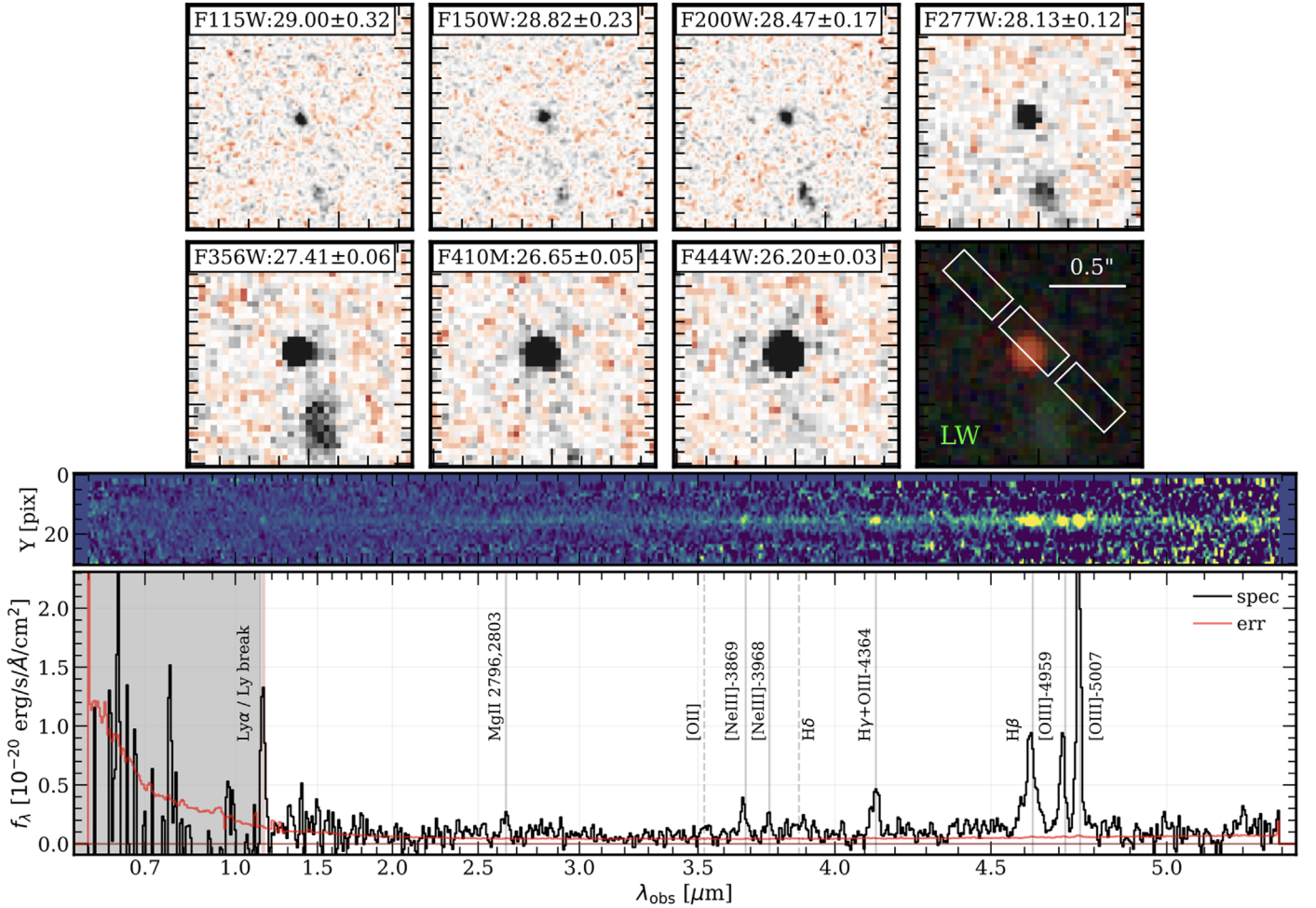


**Figure 1.** Top: JWST/NIRCam  $1''/5$  stamps and the RGB color image comprised of the F277W, F356W, and F444W bands. The MSA slitlet layout is highlighted in white. An unambiguous pointlike morphology of ID 20466 can be observed in all filters. In each panel, we show the total magnitudes with  $1\sigma$  uncertainty, as presented in the UNCOVER photometric catalog of Weaver et al. (2023). Middle: 2D MSA PRISM spectrum produced by MSAEXP. We optimally scaled the trace to highlight all of the significant line detections. Bottom: collapsed 1D spectrum of our source. We show the data in black, while the uncertainty on the spectrum is in red. Assuming the best-fit MSAEXP  $z_{\text{spec}} = 8.502 \pm 0.003$ , we show the positions of all of the prominent emission with significant ( $>3\sigma$ ) detections as solid vertical lines. Emission for which we only obtain an upper limit is shown with dashed lines.

the total photometry presented in Weaver et al. (2023). The wavelength-dependent linear correction is then computed by fitting a first-order polynomial. A complete description of the data reduction and flux calibration will be presented in S. Price et al. (2023, in preparation).

### 3. Data Analysis

#### 3.1. Spectroscopic Redshift

In order to compute the spectroscopic redshift, we use MSAEXP to fit sets of Gaussian continuum splines and emission line templates to our spectrum. As an input parameter, we set  $n_{\text{splines}}=11$  and allow it to search for the minimal  $\chi^2$  value across the wide range of  $0.1 \geq z \geq 20$ . As indicated in Figure 1, a clear Lyman break and several emission lines are clearly present in our spectrum, which results in an unambiguous redshift of  $z_{\text{spec}} = 8.502 \pm 0.003$ . This closely matches the initial redshift estimate of  $z_{\text{phot}} \sim 9$  obtained by fitting the broad- and medium-band NIRCam data (Weaver et al. 2023) with EAZY (Brammer et al. 2008).

For the analysis presented in this work, we used an updated version (v1.1) of the Furtak et al. (2023b) analytic strong lens

model of the cluster. This new model includes one additional multiple-image system in the northern substructure and, more importantly, an additional spectroscopic redshift in the north-western substructure from new VLT/MUSE observations of the cluster (Bergamini et al. 2023). Together with our secure  $z_{\text{spec}}$  for the source, we recover a magnification of  $\mu = 1.33 \pm 0.02$ .

#### 3.2. BL AGN Emission

The spectrum of our object presented in Figure 1 shows a clear broad component present in the  $H\beta$  emission line when contrasted with the narrower profiles of the adjacent [O III]  $\lambda\lambda 4959, 5007$  lines. To evaluate the potential significance of this broad feature, we perform a combined Gaussian fit to the entire line complex. For the two [O III] lines, we only consider a single narrow component, while the  $H\beta$  is fit with both narrow and broad models. We allow the velocities of the narrow and broad components to vary between 50 and 500 and 1000 and 5000  $\text{km s}^{-1}$ , respectively. In our fitting, we assume that the width of the narrow component for all three lines is the same and a fixed ratio  $[\text{O III}]_{5007}/[\text{O III}]_{4959} = 3$  (Storey & Zeppen 2000). In addition to that, we also model the local

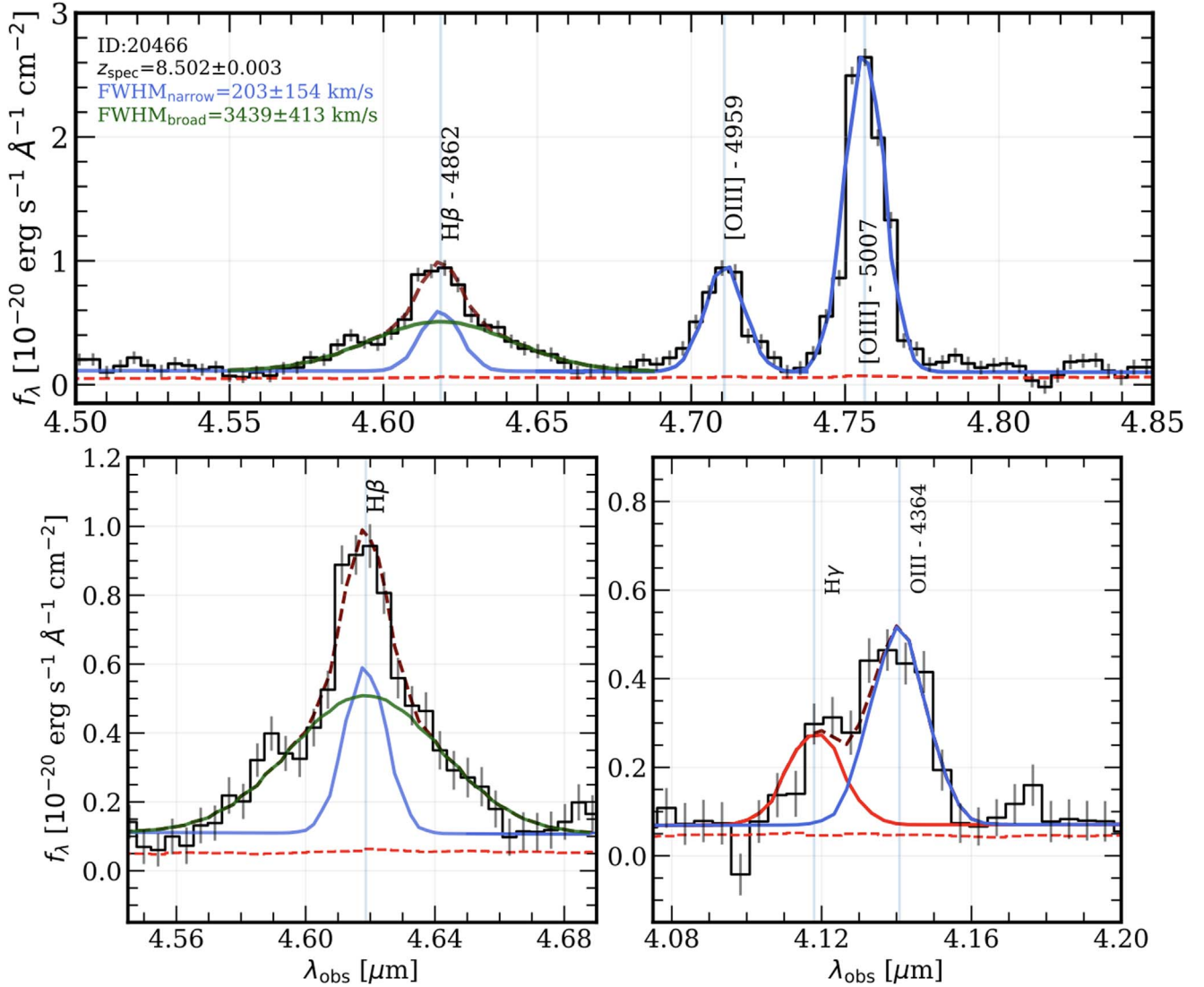


**Figure 2.** Top: best-fit narrow (blue) and broad (green) Gaussian line components fit to the H $\beta$ , [O III]  $\lambda\lambda$ 4959, 5007 line complex. A dual fit to the H $\beta$  is necessary to account for both the broad (FWHM  $\sim 3400 \text{ km s}^{-1}$ ) and narrow (FWHM  $\sim 200 \text{ km s}^{-1}$ ) components. The combined fit is shown as a dashed maroon line. The error spectrum is shown as a dashed red line. Bottom left: zoom-in on the H $\beta$  line. Bottom right: fit to the blended H $\gamma$  (red) and auroral [O III]<sub>4364</sub> (blue) lines. As before, the combined fit is shown as a dashed maroon line.

continuum with a first-order polynomial. We fix the redshift to the one obtained from MSAEXP.

We initialize the fit by first creating a set of models on the oversampled wavelength grid. To mimic the variable resolution of the PRISM, we interpolate our model onto a variable step grid while making sure that the total integrated flux is preserved. Early NIRSPEC/MSA results (de Graaff et al. 2023) have shown that the spectral resolution of a pointlike source falling within a slitlet is higher compared to a uniformly illuminated slit, sometimes up to a factor of 2. We therefore conservatively increase the nominal spectral resolution by a factor of 1.7. To take into account the effects of the line-spread function, we additionally convolve our model with a Gaussian of variable resolution (de Graaff et al. 2023; Isobe et al. 2023). The best fit is then found via nonlinear least-squares  $\chi^2$  minimization.

From our fit, we securely confirm the presence of a distinct broad component in H $\beta$  with  $\text{FWHM} = 3439 \pm 413 \text{ km s}^{-1}$ . We measure the width of the narrow component to be  $203 \pm 154 \text{ km s}^{-1}$ . In Figure 2, we show the best-fit model to

the entire line complex, with the narrow and broad components highlighted in blue and green, respectively. The flux of the broad component was measured to be  $\sim 2x$  higher than that of the narrow component.

Emission lines in AGN are typically separated into permitted (e.g., Lyman and Balmer series of hydrogen) and (semi) forbidden lines (e.g., [O III]). The distinction between the two classes is thought to arise from two physically distinct regions around an actively accreting BH (see Osterbrock 1978; Vanden Berk et al. 2001), the parsec-scale broad-line region (BLR), and the kiloparsec-scale narrow-line region (NLR). We find significant line broadening present in the H $\beta$  line, strongly hinting that some of the H $\beta$  emission originates from the BLR of a type 1 AGN. While broad emission line features can also be an indicator of large-scale outflows, if such a scenario was indeed the case, a similar broadening would be present in the forbidden [O III] lines (Amorín et al. 2012; Hogarth et al. 2020). We do not, however, find any evidence of that; on the contrary, the measured width of the narrow component is too low to be consistent with an outflow.

### 3.3. Balmer Decrement

The ratio between observed fluxes of Balmer series lines can be used to determine the dust extinction. For this purpose, we will use the  $H\beta/H\gamma$  ratio. As shown in the bottom right panel of Figure 1, the  $H\gamma$  line is blended with the  $[O\text{ III}]_{4364}$ . However, we can use the prior information from the fit to the  $H\beta+[O\text{ III}]_{4959,5007}$  complex and fix the narrow line widths to  $\sim 203\text{ km s}^{-1}$ . Similarly to  $H\beta$ , the  $H\gamma$  line would also contain a BLR component. However, the S/N of the broad component in  $H\gamma$  is too low to reliably perform a double component fit. Due to this, we assume that the primary contribution to the total  $H\gamma$  flux is coming from the NLR and compute the Balmer decrement by only considering the ratio between the narrow component of the  $H\beta$  line and our derived  $H\gamma$  flux. In this case, we ensure that both line fluxes are obtained by integrating similar velocity ranges. From this calculation, we find  $H\beta/H\gamma = 3.2^{+0.7}_{-0.5}$ .

To compute the  $A_V$ , we adopt the Small Magellanic Cloud (SMC) reddening law (Gordon et al. 2003), which has been found to match well the dust attenuation in high- $z$  galaxies (Capak et al. 2015; Reddy et al. 2015, 2018) and reddened quasars (e.g., see Hopkins et al. 2004). Given Case B recombination, the intrinsic ratio between the lines is  $(H\beta/H\gamma)_{\text{int}} = 2.14$  (Osterbrock 1989). We find that the observed line ratio implies a high attenuation of  $A_V = 2.1^{+1.1}_{-1.0}$ .

### 3.4. Template Fitting

While it is likely that the contribution from the host galaxy to the total flux is small, as indicated by the mostly point source-like morphology of the source, obtaining an upper limit on the  $M_*$  can still yield some crucial clues regarding the nature of our source. We follow the joint template fitting procedure described in Labbé et al. (2023a), fixing the redshift at  $z_{\text{spec}} = 8.502$ . Briefly, the Labbé et al. method employs a custom fitting procedure that combines dust-obscured stellar population models from FSPS (Conroy et al. 2009) with empirical AGN models based on composite optical/near-infrared spectra of Sloan Digital Sky Survey (SDSS) quasars (Vanden Berk et al. 2001; Glikman et al. 2006). To fit the stellar population, we utilize three independent FSPS models: dust-free and dust-obscured star-forming components together with an old quiescent component. A constant star formation history (SFH) is assumed for the star-forming components, while the quiescent part uses an exponentially declining SFH with  $\tau = 1\text{ Myr}$ . These templates are reddened by  $A_V = 0-5$  using a Calzetti (2001) attenuation law and  $R_V = 3.1$ . The attenuated AGN light is reemitted in the mid-to-far-infrared and modeled with the CLUMPY torus models (Nenkova et al. 2008a, 2008b) as included with FSPS. The far-infrared dust emission associated with dust-obscured star formation is based on a set of Draine et al. (2007) templates employed within FSPS. NIRSPEC observations are simulated using the published line-spread function increased by a factor of 1.4 to account for the fact that this is a point source. For a full description of the fitting procedure, assumptions, and potential caveats, please refer to Appendix A in Labbé et al. (2023a).

With these models, we fit the NIRCAM spectroscopy, all available NIRCAM broad- and medium-band photometry, and the point-source flux from Atacama Large Millimeter/submillimeter Array (ALMA) Band 6 at 1.2 mm (Fujimoto et al. 2023a, 2023b) extracted using the NIRCAM location as a prior.

**Table 1**  
Source Properties<sup>a</sup>

R.A.	3.640408
Decl.	−30.386438
$z_{\text{spec}}$	$8.502 \pm 0.003$
$z_{\text{phot}}$ <sup>b</sup>	$9.0 \pm 0.3$
$\mu$	$1.33 \pm 0.02$
$A_V(H\beta/H\gamma)$ [mag]	$2.1^{+1.1}_{-1.0}$
$A_V(\text{continuum})$ [mag]	$\sim 1.9$
$\log_{10}(M_*/M_\odot)$	$< 8.7$
$\text{FWHM}_{\text{narrow}}$ [km s <sup>−1</sup> ]	$203 \pm 154$
$\text{FWHM}_{\text{broad}}$ [km s <sup>−1</sup> ]	$3439 \pm 413$
$\log_{10}(M_{\text{BH}}/M_\odot)$ ( $H\beta$ )	$8.17 \pm 0.42$
$\log_{10}(M_{\text{BH}}/M_\odot)$ ( $L_{5100}$ )	$8.01 \pm 0.40$
$L_{\text{bol}}$ [erg s <sup>−1</sup> ]	$(6.6 \pm 3.1) \times 10^{45}$
$L_{\gamma\alpha}$ EW <sub>0</sub> [Å]	$240 \pm 30$

**Notes.**

<sup>a</sup> Corrected for the lensing magnification.

<sup>b</sup> From the latest UNCOVER v3.0.1 catalog.

No flux is detected in ALMA to  $< 70\ \mu\text{Jy}$  ( $2\sigma$ ), which strongly limits the contribution of massive star formation (see Labbé et al. 2013).

Three types of model fits are performed: AGN-only, AGN+stars, and stars-only. The AGN-only model fits a separate unreddened blue and reddened AGN template. Two templates are needed because of the remarkable dichotomy that the SEDs of typical “little red dots” display, where the SED at 1–2  $\mu\text{m}$  (1000–1000 Å rest) is blue ( $f_\lambda \propto \lambda^{-2}$ ), while the SED at 3–5  $\mu\text{m}$  (3100–5200 Å rest) is red ( $f_\lambda \propto \lambda^{0-2}$ ).

The best-fit blue component is only  $\sim 1\%$  of the bolometric luminosity of the red component, consistent with being scattered AGN light. The absence of clearly detectable broad UV lines (e.g., C IV, Mg II) is consistent with expectations from the blue SDSS QSO template given the simulated NIRSPEC PRISM resolution and depth. The best-fit dust attenuation is  $A_V \sim 1.9$  when converted from Calzetti (2001) to the SMC law with  $R_V = 2.7$ , consistent with estimates based on the Balmer decrement.

Next, joint AGN+stars fits are performed. These should yield the most realistic constraint on the stellar mass from an underlying host galaxy. From these joint fits, we derive an upper limit on the stellar mass of  $\log_{10}(M_*/M_\odot) < 8.3$  based on the 95th percentile of the posterior distribution of the mass of the stellar components. The stellar mass is primarily constrained by the combination of red NIRCAM colors and the ALMA nondetection, which limits the amount of cold dust emission. We also note that evolved stellar populations are not seen in our spectrum due to the lack of a Balmer break. As such, the red continuum will most likely correspond to the dusty star formation, therefore allowing ALMA to further constrain the shape of our SED (see Labbé et al. 2023a for further details). To derive an upper limit on the stellar mass, we assume that all emission originates from stars. For the stars-only fit, we find  $\log_{10}(M_*/M_\odot) < 8.7$  based on the 95% of the posterior on the total stellar mass. We adopt this as a conservative upper limit on the  $M_*$ . We list the stellar mass alongside other properties in Table 1.

As an additional test, we hypothesize what could be the maximum amount of  $M_*$  present in this object if we assume a more evolved stellar population and ignore the observed shape of the SED. For this, we use a dust-free model based on the

**Table 2**  
Measured Line Fluxes

Line	$\lambda_{\text{rest}}$ (Å)	Flux ( $10^{-20}$ erg s $^{-1}$ cm $^{-2}$ )
Ly $\alpha$	1215.4	414.1 $\pm$ 85.2
Mg II	2796.5, 2803.1	62.5 $\pm$ 15.1
[O II]	3727.0, 3729.9	15.2 $\pm$ 8.0
[Ne III]	3869.9	62.2 $\pm$ 15.4
[Ne III]	3968.6	38.9 $\pm$ 9.2
H $\delta$	4102.9	12.2 $\pm$ 6.5
H $\gamma$ (narrow+broad)	4341.7	24.6 $\pm$ 3.1
[O III]	4364.4	83.0 $\pm$ 7.2
H $\beta$ (narrow)	4862.7	78.6 $\pm$ 5.9
H $\beta$ (broad)	4862.7	232.6 $\pm$ 17.3
[O III]	4959.5	136.7 $\pm$ 3.0
[O III]	5007.2	412.6 $\pm$ 11.3

exponentially declining SFH ( $\tau = 1$  Myr) that formed 300 Myr ago at  $z \sim 15$ . This is then scaled directly to the depth of our NIRCcam images at the position of 20466 (Weaver et al. 2023). The resulting limit is then  $\log_{10}(M_*/M_\odot) < 9.3$ . We note, however, that such a model is not consistent with the photometry or the spectrum.

Finally, it is also possible to envision that the AGN can be embedded within an extremely dusty galaxy that surrounds the object and yet remains completely JWST-dark due to dust obscuration and low surface brightness. The implications of such dusty galaxies existing at high  $z$  were briefly explored in Kokorev et al. (2023), who presented an overview of a highly obscured ( $A_V \sim 4$ ) galaxy at  $z = 2.58$ . By adapting the full UV-to-submillimeter SED from Kokorev et al. and scaling it to our ALMA photometry, we compute a stellar mass limit of  $\log_{10}(M_*/M_\odot) < 9.5$ . This might be an overestimate because the low redshift has a best-fit stellar age of 0.53 Gyr, implying that all mass is formed at  $z = 50$ , which is not realistic. While definitive evidence for a significant presence of dust in galaxies only 500 Myr after the Big Bang is still lacking, deeper NIRCcam observations of lensed fields could assist in uncovering the diffuse and dusty host galaxies surrounding red-denied AGN.

### 3.5. Other Emission Lines

Beyond the lines discussed in earlier sections, our spectrum reveals emissions from Ly $\alpha$ , the Mg II doublet, and [Ne III]  $\lambda\lambda 3869, 3968$ . In this section, we outline the methods and underlying assumptions employed to determine the final flux of each line. All measured line fluxes can be found in Table 2.

The Ly $\alpha$  is fit with a single Gaussian model, where the FWHM is allowed to vary. Using this fit, we extract both the line intensity and the rest-frame equivalent width ( $EW_0$ ), with the latter being measured at  $240 \pm 30$  Å.

In our spectrum, we identify the Mg II  $\lambda\lambda 2796, 2804$  doublet feature. It is expected that, similarly to H $\beta$ , this permitted transition will contain both the narrow and broad components. However, the spectral resolution of PRISM at the observed wavelength of Mg II does not allow us to securely separate the lines and perform a multiple-component fit. We therefore fit the doublet with a single Gaussian model, where the FWHM is allowed to vary.

The [Ne III]  $\lambda\lambda 3869, 3968$  lines are nicely separated in our spectrum, as seen in Figure 1. As discussed previously, the emission from the forbidden lines is generally expected to arise

from the NLR (Vanden Berk et al. 2001); as such, we fix the FWHM of [Ne III] to be the same as that of [O III]  $\lambda\lambda 4959, 5007$ .

In addition to the detected lines, we also report a  $3\sigma$  upper limit for the low-S/N ( $< 3$ ) [O II]  $\lambda\lambda 3727, 3729$  doublet and H $\delta$ .

### 3.6. Size Measurement

As can be seen in Figure 1, the source is very compact and just barely resolved in our imaging. We measure the effective radius in all available JWST bands using GALFIT (Peng et al. 2002, 2010), accounting for the effect of the empirically measured (Weaver et al. 2023) point-spread function (PSF). The light is modeled with a Sérsic profile with the center, brightness, effective radius, Sérsic index, and axis ratio as free parameters. From the best fits, we find that the measured sizes in the short-wavelength bands (F115W, F150W, F200W) are comparable to the ones at long wavelengths (F277W, F356W, F410M, F444W) and range from  $0''.035$  to  $0''.04$ , which is consistent with or even smaller than the FWHM of the NIRCcam PSF for those bands. The consistency of sizes across all bands, coupled with a pure PSF fit being sufficient to describe the light from 20466, provides further evidence of the high degree of central concentration in our object. Finally, we derive a physical effective radius of  $165 \pm 20$  pc when corrected for the lensing magnification.

## 4. Results

### 4.1. AGN Properties

Reverberation mapping of quasars has revealed a correlation between the distance to the BLR in AGN and the width of the H $\beta$  line (e.g., Kaspi et al. 2000; Greene & Ho 2005), which allows for the BH mass to be estimated from single-epoch measurements. Using the standard relations presented in Greene & Ho (2005), we compute the BH mass ( $M_{\text{BH}}$ ) from both the luminosity and the width of the broad component of the H $\beta$  line and the rest-frame  $L_{5100}$  luminosity of the continuum.

Using our best-fit models for lines and the continuum and accounting for the effects of lensing and dust obscuration, we find  $\log_{10}(M_{\text{BH,H}\beta}/M_\odot) = 8.17 \pm 0.42$  and  $\log_{10}(M_{\text{BH},5100}/M_\odot) = 8.01 \pm 0.40$ . The uncertainties in this case are primarily dominated by the scatter ( $\sim 0.3$  dex) in the virial relation used to derive the mass, rather than the errors on the measurements themselves (e.g., see Kollmeier et al. 2006). From the fact that both methods return a consistent result, we can conclude that the rest-frame 5100 Å luminosity of 20466 is almost entirely dominated by the light from the AGN. This allows us to further justify the assumptions made when modeling the spectrum in Section 3.4. We adopt the  $M_{\text{BH}}$  derived from the H $\beta$  line luminosity as our final result.

In addition to the mass, the broad H $\beta$  can be used to compute the bolometric luminosity ( $L_{\text{bol}}$ ) of the AGN. Typically,  $L_{\text{bol}}$  is computed from the luminosity of H $\alpha$ , which we lack. However, we can assume a BL intrinsic ratio of  $H\alpha/H\beta \sim 3.06$  (Dong et al. 2008) and use it in conjunction with  $L_{\text{bol}} = 3.06 \times 130 \times L_{\text{H}\beta}$  (Richards et al. 2006; Stern & Laor 2012). Assuming that the dust attenuation within the NLR and BLR are similar, we correct the H $\beta$  luminosity for dust attenuation and magnification effects, thus obtaining  $L_{\text{bol}} = (6.6 \pm 3.1) \times 10^{45}$  erg s $^{-1}$ . These results suggest that our object is accreting at  $\sim 40\%$  of the Eddington

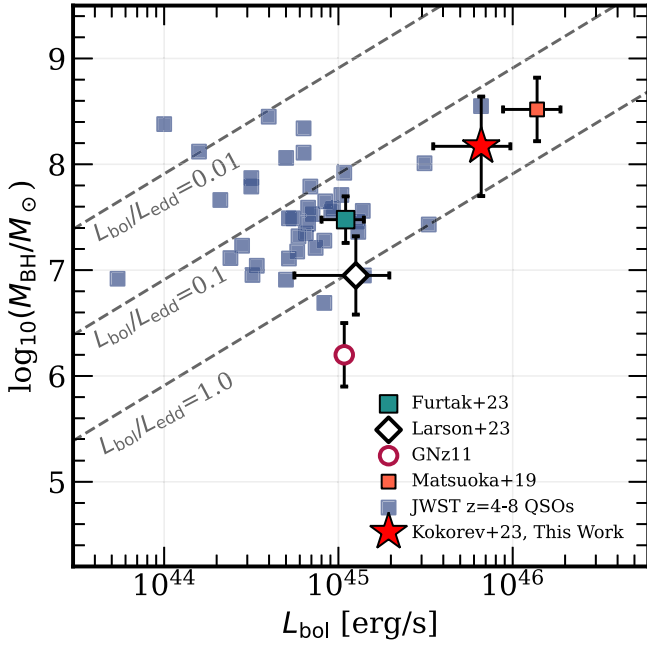


**Figure 3.** Derived  $M_{\text{BH}}$  and  $L_{\text{bol}}$  compared to the other high- $z$  quasars. Our source is shown as a red star. Two high- $z$  AGN candidates, CEERS\_1019 at  $z = 8.7$  (Larson et al. 2023) and GNz11 at  $z = 10.6$  (Maiolino et al. 2023b), are shown as an open diamond and circle, respectively. JWST-detected AGN at  $z > 4$  are shown as blue squares (Harikane et al. 2023; Kocevski et al. 2023; Maiolino et al. 2023a; Matthee et al. 2023). The cyan square shows the triply lensed quasar from Furtak et al. (2023a). A massive, bright  $z = 7.07$  QSO from Matsuoka et al. (2019) is shown as an orange square. The dashed lines show the bolometric luminosities with Eddington ratios of  $L_{\text{bol}}/L_{\text{edd}} = 0.01, 0.1,$  and  $1.0$ .

rate, with  $L_{\text{bol}}/L_{\text{edd}} \sim 0.4$ , suggesting a sub-Eddington accretion scenario. All of the estimated parameters are presented in Table 1.

In Figure 3, we show the estimated  $M_{\text{BH}}$  and  $L_{\text{bol}}$  for our object. A mass exceeding  $10^8 M_{\odot}$  and luminosity brighter than  $5 \times 10^{45} \text{ erg s}^{-1}$  indicate that our source is more massive and luminous than the majority of quasars at the  $z \sim 4\text{--}8$  range identified with JWST (Furtak et al. 2023a; Harikane et al. 2023; Kocevski et al. 2023). The object presented in Larson et al. (2023) at  $z \sim 8.7$  is only  $\sim 20$  Myr younger; however, it shows an almost 1 dex difference in the derived BH mass. This suggests that CEERS\_1019 and 20466 might have followed vastly different evolutionary scenarios. On the other hand, we find a similar (within  $1\sigma$ ) mass and luminosity when compared to the  $z = 7.07$  quasar presented in Matsuoka et al. (2019).

#### 4.2. Ionization Mechanisms

In this section, we briefly explore the ratios between the measured emission lines to investigate the potential ionization mechanisms in our source. We observe an unusually high ratio between the auroral  $[\text{O III}]_{4364}$  line and  $[\text{O III}]_{5007}$  (RO3) of 0.32. In Figure 4, we explore the typical “allowed” RO3 for a range of electron temperatures  $T_e$  and densities  $n_e$  from the models presented in Nicholls et al. (2020) alongside our observed and dust-corrected RO3. When compared to the models, our object appears to be a significant outlier, regardless of the adopted  $T_e$  and  $n_e$  values. Extreme values of RO3 have already been reported in recent JWST spectra; for example, a  $z = 8.5$  galaxy presented in Katz et al. (2023) shows an RO3 of 0.048 when corrected for dust. Elevated RO3s are not new and have been discussed in the context of low- $z$  Seyfert galaxies

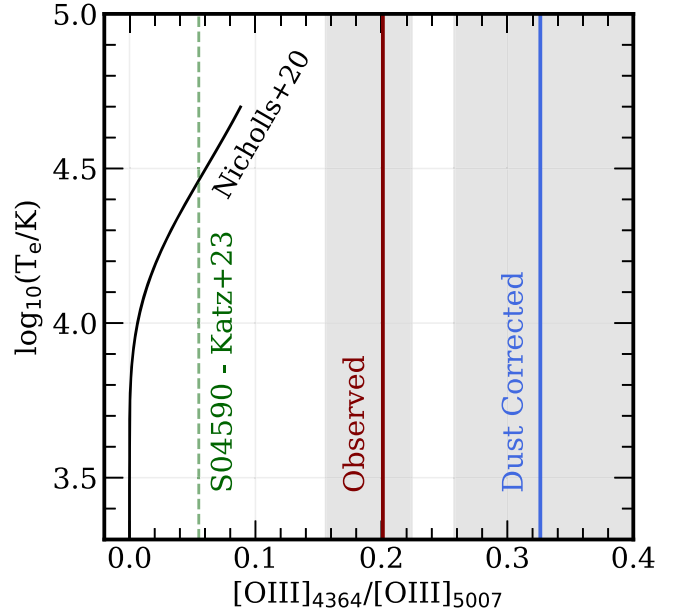


**Figure 4.** Electron temperature ( $T_e$ ) as a function of the  $[\text{O III}]_{4364}/[\text{O III}]_{5007}$  (RO3) ratio. In black, we present models from Nicholls et al. (2020) for different electron densities ranging from 1 to  $10^4$ ; the dynamic range does not allow us to distinguish between different lines, however. We show our observed line ratio in maroon, as well as in blue after the dust correction. The  $z = 8.5$  source displaying extreme RO3 from Katz et al. (2023) is shown with a dashed green line. The shaded regions show the  $1\sigma$  uncertainty. The extremely high line ratio we find is indicative of AGN-dominated ionization.

(e.g., Koski & Osterbrock 1976; Osterbrock 1978; Ferland & Netzer 1983; Dopita & Sutherland 1995; Nagao et al. 2001; Baskin & Laor 2005; Binette et al. 2022). In fact, the photoionization models of Baskin & Laor (2005) suggest that it is possible to reach the required densities and temperatures to produce extreme RO3s within the NLR around an AGN.

In addition, we can investigate our source in the context of the often-utilized “OHNO” diagnostic, which compares the  $[\text{O III}]_{5007}/\text{H}\beta$  and  $[\text{Ne III}]_{3869}/[\text{O II}]_{3727,3729}$  ratios. This diagnostic has been used at low and high  $z$  to ascertain whether the ionization is powered purely by star formation or by an AGN (Backhaus et al. 2022; Cleri et al. 2022; Larson et al. 2023). After dust correction, we find  $\log_{10}([\text{O III}]_{5007}/\text{H}\beta) \sim 0.68$  and a lower limit of  $\log_{10}([\text{Ne III}]_{3870}/[\text{O II}]) > 0.15$ . These line ratios, while not as high as reported in other  $z > 8$  AGN candidates (Larson et al. 2023), are still indicative of high ionization in 20466.

#### 4.3. Massive Accreting BH at $z = 8.50$

With all of the information in hand, we would like to remark on the most probable nature of our source. The spectrum of 20466 shows a clear BL component present in the  $\text{H}\beta$  line. With a confidence level of  $13.4\sigma$ , we estimate the FWHM of the broad profile to be  $\sim 3440 \text{ km s}^{-1}$ . The adjacent  $[\text{O III}]$  lines are well fit with a much narrower Gaussian ( $\sim 200 \text{ km s}^{-1}$ ), ruling out potential outflows (e.g., see Chisholm et al. 2015). This leads us to conclude that broad  $\text{H}\beta$  emission most likely originates within a BLR of an AGN. Furthermore, we note the high ionization present in our source, as indicated by the extreme RO3 ratio, as well as the OHNO diagnostic. These values are difficult to reconcile with photoionization by young stars alone, highlighting the strong ionizing nature of this source. Combining the above with the nearly pointlike source

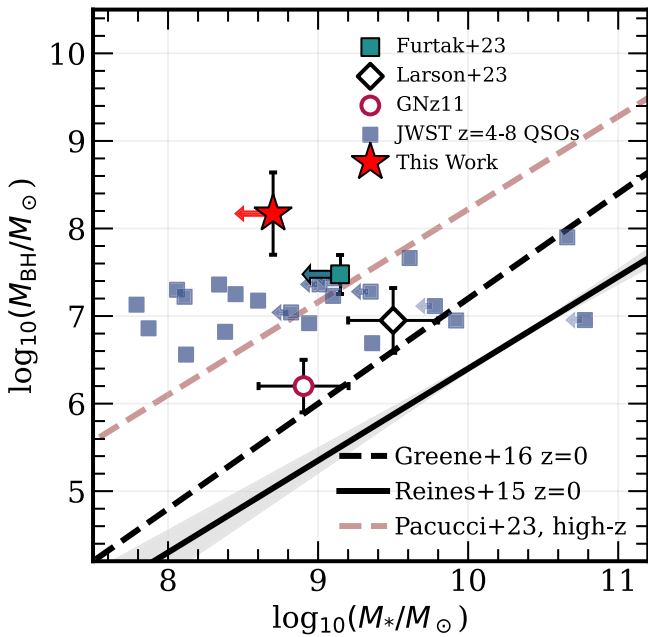


**Figure 5.** BH-to-stellar mass relation. The color coding is the same as in Figure 3. The solid and dashed black lines show the best fits to the  $z=0$  AGN samples from Reines & Volonteri (2015) and Greene et al. (2016), respectively. The high- $z$  trend from Pacucci et al. (2023) is shown as a dashed maroon line. Only an upper limit on  $M_*$  is available for our source and the triply lensed quasar from Furtak et al. (2023a).

morphology observed across all NIRCcam bands leads us to conclude that 20466 is a massive and luminous type 1 AGN observed just 580 Myr after the Big Bang.

## 5. Discussion and Conclusion

### 5.1. BH Formation Mechanisms

A significant unresolved question that remains to be answered is how these SMBHs come to be. In Figure 5, we present the  $M_{\text{BH}}$  versus an upper limit on the  $M_*$ , derived from the template fitting, compared to the relations for QSOs at  $z \sim 0$ , JWST-detected AGN at  $z=4-5$ , and those recently identified at high  $z$ . We find an extremely high ratio of BH-to-host mass of at least  $\sim 30\%$ , which is orders of magnitude higher compared to the local QSOs, and also elevated when compared to other massive AGN at high  $z$ . Predictions from DCBH formation models suggest that this ratio can indeed be high close to the seeding epoch (Natarajan 2011; Natarajan et al. 2017) compared to the local values. Moreover, reaching a high  $M_{\text{BH}}/M_*$  from light seeds would require growing the  $M_{\text{BH}}$  without also growing the galaxy mass, which does not seem feasible. This gives us a first hint regarding the potential formation and accretion mechanisms of our source.

We further explore this in Figure 6, which presents the  $M_{\text{BH}}$  as a function of cosmic age for our AGN, alongside previous measurements for high- $z$  QSOs. It is possible to explain the existence of these SMBHs via the super-Eddington accretion rates (e.g., Haiman & Loeb 2001; Alexander & Natarajan 2014) in low-mass BH seeds ( $\sim 100 M_\odot$ ) formed from Population III stars (Madau & Rees 2001). Another possible solution is to start from heavy DCBH seeds,  $\sim 10^{3-5} M_\odot$ , from the collapse of pristine gas in early halos (e.g., Rees 1984; Loeb & Rasio 1994). In this work, we consider both options; starting with low- ( $100 M_\odot$ ) and high- ( $10^4 M_\odot$ ) mass seeds at  $z \sim 50$ ,

we explore the different accretion rates required to grow a BH to  $10^8 M_\odot$  by  $z = 8.5$ . In Figure 6, we show that the observed  $M_{\text{BH}}$  can be reproduced by continuous Eddington-driven growth in a DCBH seed at  $10^4 M_\odot$ , with the Eddington-limited stellar mass seed scenario being unlikely. Furthermore, it would be difficult to explain a radical change in  $M_{\text{BH}}/M_*$  over these early times, which would naively mean that the high BH-to-galaxy ratio that we find also favors heavy seeds. Alternatively, simulations show that it is also possible to grow an SMBH via super-Eddington accretion onto a stellar mass seed (Jeon et al. 2012; Massonneau et al. 2023); however, the feasibility of such extreme accretion modes is yet to be conclusively determined.

Recent detection and NIRSpc observations of an X-ray quasar at  $z = 10.07$ , UHZ-1 (Bogdan et al. 2023; Goulding et al. 2023), find  $M_{\text{BH}}/M_* \sim 5\% - 100\%$ , comparable to the ratio we derive in this work. MSA ID 20466 and UHZ-1 are located in the same field, in a relatively small area, which suggests that BHs that form from direct collapse could be more common than previously thought, and some early overmassive SMBHs may indeed originate from heavy seeds (Eilers et al. 2023; Natarajan et al. 2023; Pacucci et al. 2023; Stone et al. 2023).

However, we note that the elevated  $M_{\text{BH}}$ -to-host stellar mass trends might not manifest when using the dynamical mass of the galaxy instead. A recent work by Maiolino et al. (2023a) finds little deviation between the  $M_{\text{BH}}-M_{\text{dyn}}$  relation in  $z > 4$  BL AGN and that of local QSOs. This, in turn, might imply that BH formation is more strongly connected with the mass assembly itself, rather than star formation in the host galaxy.

### 5.2. Final Remarks

Using the NIRSpc/PRISM and NIRCcam data from the JWST UNCOVER survey, we present the discovery of an actively accreting SMBH at  $z = 8.502 \pm 0.003$ . The spectrum of our object shows an unambiguous ( $> 10\sigma$ ) BL component present in the  $\text{H}\beta$  line exhibiting an FWHM of  $\sim 3400 \text{ km s}^{-1}$ . Although comparable velocities could potentially stem from large-scale outflows, a corresponding broadening effect should manifest in the adjacent  $[\text{O III}]_{4959}$  and  $[\text{O III}]_{5007}$  lines. We do not, however, find any evidence that can support this. By examining the RO3 and the OHNO line diagnostic, we find values that are consistent with the high ionization present in the source. These findings, compounded by nearly point-source morphology, lead us to deduce that the underlying cause of the extended BLR can only be attributed to AGN activity.

From the flux and FWHM of the  $\text{H}\beta$ , we compute a BH mass of  $\log_{10}(M_{\text{BH}}/M_\odot) = 8.17 \pm 0.42$  and a luminosity of  $L_{\text{bol}} = 6.6 \pm 3.1 \text{ erg s}^{-1}$ , suggesting an accretion rate at  $\sim 40\%$  of the Eddington limit. We also find that the  $M_{\text{BH}}$  derived from the  $\text{H}\beta$  is consistent with that computed from the rest-frame  $5100 \text{ \AA}$  continuum within one standard deviation, potentially indicating that the spectrum of this object is strongly or almost entirely dominated by the AGN emission.

Finally, we explore multiple scenarios that can lead to the presence of such a massive BH by  $z = 8.50$ . We find that the BH mass cannot be reproduced by Eddington-limited accretion from a stellar seed unless super-Eddington regimes can be achieved. It is worth noting that this would require a gas-rich disk providing material for accretion while remaining unaffected by BH feedback. Even in our models that start at  $z = 50$ , this SMBH would need to grow at sustained rates for



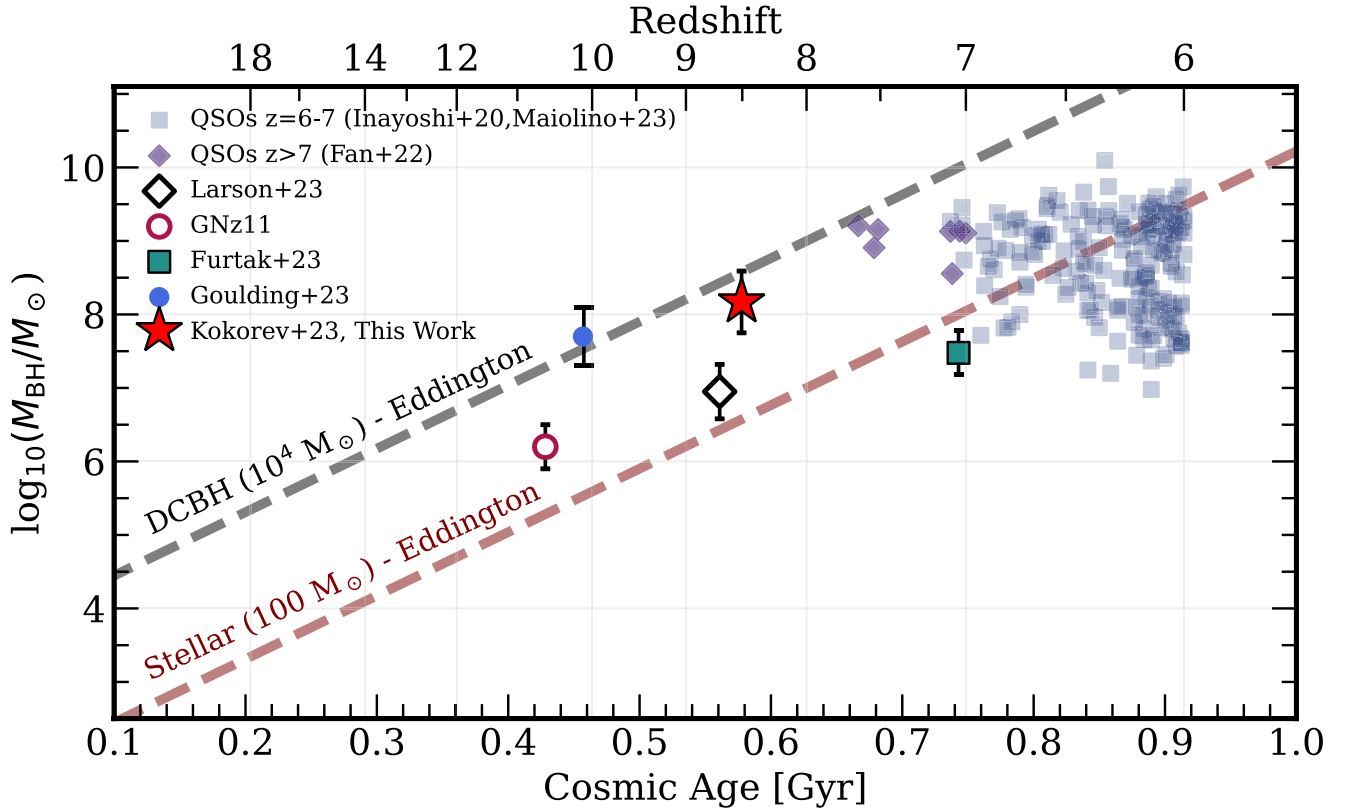


**Figure 6.** BH mass vs. cosmic age. The red star shows the result presented in this work. The dark blue squares and violet diamonds show the results for  $z = 6-7$  and  $>7$  QSOs, respectively, as presented in Inayoshi et al. (2020), Maiolino et al. (2023a), and Fan et al. (2023). A triply lensed  $z = 7$  QSO from Furtak et al. (2023a) is shown as a cyan square. A tentative  $M_{\text{BH}}$  range for UHZ-1 at  $z = 10.1$  from Goulding et al. (2023) is shown as a blue circle. Two high- $z$  AGN candidates, namely,  $z = 8.7$  AGN from CEERS (Larson et al. 2023) and GNz11 at  $z = 10.6$  (Maiolino et al. 2023b), are shown as an open diamond and circle, respectively. Dashed lines show analytical models of BH mass accretion at an Eddington rate starting from a stellar seed (maroon) and a DCBH model (black).

$>400$  Myr, all the while remaining in a super-Eddington regime, which is beyond physically plausible scenarios. On the other hand, such a mass can also be attained via Eddington accretion-driven growth for DCBH ( $\sim 10^4 M_{\odot}$ ) seeds. A direct-collapse model would then also be able to potentially explain the extreme BH-to-host ratio of at least  $\sim 30\%$  found in our source.

While their formation pathways are still largely uncertain, the high number of AGN detected with JWST at high  $z$ , given the relatively small areas covered so far, implies that extremely massive SMBHs are already in place at  $z > 7$ , just  $\sim 700$  Myr after the Big Bang (Wang et al. 2021; Furtak et al. 2023a; Goulding et al. 2023; Greene et al. 2023; Larson et al. 2023; Pacucci et al. 2023). The clue of high BH-to-stellar mass ratios exceeding several tens of percent will allow us to place stronger constraints on the sizes of the BH seeds and accretion modes required to produce such massive objects (Bogdan et al. 2023; Goulding et al. 2023). Interestingly, the Ly $\alpha$  line is clearly detected from 20466 despite its heavily dusty nature, and 20466 turns out to reside in a huge ionized bubble with a radius of 7.6 proper Mpc (Fujimoto et al. 2023c). These results may indicate that the recent abundant AGN population identified with JWST provides a nonnegligible contribution of ionizing flux to cosmic reionization. It is also possible that these AGN are residing in galaxy overdensities, which may have reionized the Universe earlier in their environments. The identification of 20466, along with similar massive quasars at high  $z$ , suggests that we still lack a comprehensive understanding of AGN and

host galaxy coevolution in the early Universe, which we only recently started exploring with JWST.

### Acknowledgments


We thank the anonymous referee for a number of constructive suggestions, which helped to improve this manuscript. We thank Darach Watson and Maxime Trebitsch for insightful discussions on black hole physics. We are also grateful to Katriona Gould for helpful discussions about MSAEXP. We would like to thank Alex Pope for useful discussions regarding dusty star formation. V.K. and K.I.C. acknowledge funding from the Dutch Research Council (NWO) through the award of Vici grant VIC.212.036. A.Z. acknowledges support by grant No. 2020750 from the United States–Israel Binational Science Foundation (BSF), grant No. 2109066 from the United States National Science Foundation (NSF), and the Ministry of Science & Technology, Israel. I.L. acknowledges support by the Australian Research Council through Future Fellowship FT220100798. P.D. acknowledges support from the Dutch Research Council (NWO) through the award of VIDI grant 016.VIDI.189.162 (“ODIN”) and the European Commission’s and University of Groningen’s CO-FUND Rosalind Franklin program. H.A. and I.C. acknowledge support from CNES, focused on the JWST mission, and the Programme National Cosmology and Galaxies (PNCG) of CNRS/INSU with INP and IN2P3, cofunded by CEA and CNES. R.P. and D.M. acknowledge support from JWST-GO-02561.013-A. Y.F. acknowledges support from NAOJ ALMA Scientific Research grant No. 2020-16B. Y.F.

further acknowledges support from JSPS KAKENHI grant No. JP23K13149. M.S. acknowledges support from the CIDE-GENT/2021/059 grant from project PID2019-109592GB-I00/AEI/10.13039/501100011033 from the Spanish Ministerio de Ciencia e Innovación—Agencia Estatal de Investigación. M.S.T. also acknowledges the financial support from the MCIN with funding from the European Union NextGenerationEU and Generalitat Valenciana in the Programa de Planes Complementarios de I + D + i (PRTR 2022) Project (VAL-JPAS), reference ASFAE/2022/025. This work is based on observations made with the NASA/ESA/CSA James Webb Space Telescope. The data were obtained from the Mikulski Archive for Space Telescopes at the Space Telescope Science Institute, which is operated by the Association of Universities for Research in Astronomy, Inc., under NASA contract NAS 5-03127 for JWST. These observations are associated with program JWST-GO-2561. Support for program JWST-GO-2561 was provided by NASA through a grant from the Space Telescope Science Institute, which is operated by the Association of Universities for Research in Astronomy, Inc., under NASA contract NAS 5-03127. This work has received funding from the Swiss State Secretariat for Education, Research and Innovation (SERI) under contract No. MB22.00072, as well as the Swiss National Science Foundation (SNSF) through project grant 200020\_207349. The Cosmic Dawn Center (DAWN) is funded by the Danish National Research Foundation under grant No. 140. The work of C.C.W. is supported by NOIRLab, which is managed by the Association of Universities for Research in Astronomy (AURA) under a cooperative agreement with the National Science Foundation.

*Facilities:* JWST, ALMA.

*Software:* EAZY (Brammer et al. 2008), FSPS (Conroy et al. 2009), GALFIT (Peng et al. 2002, 2010), grizli (Brammer 2023), msaexp (Brammer 2022).

### ORCID iDs

Vasily Kokorev  <https://orcid.org/0000-0002-5588-9156>  
 Seiji Fujimoto  <https://orcid.org/0000-0001-7201-5066>  
 Ivo Labbe  <https://orcid.org/0000-0002-2057-5376>  
 Jenny E. Greene  <https://orcid.org/0000-0002-5612-3427>  
 Rachel Bezanson  <https://orcid.org/0000-0001-5063-8254>  
 Pratika Dayal  <https://orcid.org/0000-0001-8460-1564>  
 Erica J. Nelson  <https://orcid.org/0000-0002-7524-374X>  
 Hakim Atek  <https://orcid.org/0000-0002-7570-0824>  
 Gabriel Brammer  <https://orcid.org/0000-0003-2680-005X>  
 Karina I. Caputi  <https://orcid.org/0000-0001-8183-1460>  
 Iryna Chemerynska  <https://orcid.org/0009-0009-9795-6167>  
 Sam E. Cutler  <https://orcid.org/0000-0002-7031-2865>  
 Robert Feldmann  <https://orcid.org/0000-0002-1109-1919>  
 Yoshinobu Fudamoto  <https://orcid.org/0000-0001-7440-8832>  
 Lukas J. Furtak  <https://orcid.org/0000-0001-6278-032X>  
 Andy D. Goulding  <https://orcid.org/0000-0003-4700-663X>  
 Anna de Graaff  <https://orcid.org/0000-0002-2380-9801>  
 Joel Leja  <https://orcid.org/0000-0001-6755-1315>  
 Danilo Marchesini  <https://orcid.org/0000-0001-9002-3502>  
 Tim B. Miller  <https://orcid.org/0000-0001-8367-6265>  
 Themiyana Nanayakkara  <https://orcid.org/0000-0003-2804-0648>  
 Pascal A. Oesch  <https://orcid.org/0000-0001-5851-6649>  
 Richard Pan  <https://orcid.org/0000-0002-9651-5716>  
 Sedona H. Price  <https://orcid.org/0000-0002-0108-4176>  
 David J. Setton  <https://orcid.org/0000-0003-4075-7393>

Renske Smit  <https://orcid.org/0000-0001-8034-7802>  
 Mauro Stefanon  <https://orcid.org/0000-0001-7768-5309>  
 Bingjie Wang (王冰洁)  <https://orcid.org/0000-0001-9269-5046>  
 John R. Weaver  <https://orcid.org/0000-0003-1614-196X>  
 Katherine E. Whitaker  <https://orcid.org/0000-0001-7160-3632>  
 Christina C. Williams  <https://orcid.org/0000-0003-2919-7495>  
 Adi Zitrin  <https://orcid.org/0000-0002-0350-4488>

### References

- Alexander, T., & Natarajan, P. 2014, *Sci*, **345**, 1330  
 Amorín, R., Pérez-Montero, E., Vilchez, J. M., & Papaderos, P. 2012, *ApJ*, **749**, 185  
 Backhaus, B. E., Trump, J. R., Cleri, N. J., et al. 2022, *ApJ*, **926**, 161  
 Bañados, E., Carilli, C., Walter, F., et al. 2018, *ApJL*, **861**, L14  
 Barro, G., Perez-Gonzalez, P. G., Kocevski, D. D., et al. 2023, arXiv:2305.14418  
 Baskin, A., & Laor, A. 2005, *MNRAS*, **358**, 1043  
 Bergamini, P., Acebron, A., Grillo, C., et al. 2023, *ApJ*, **952**, 84  
 Bezanson, R., Labbe, I., Whitaker, K. E., et al. 2022, arXiv:2212.04026  
 Binette, L., Villar Martín, M., Magris, C. G., et al. 2022, *RMxAA*, **58**, 133  
 Bogdan, A., Goulding, A., Natarajan, P., et al. 2023, arXiv:2305.15458  
 Brammer, G. 2022, msaexp: NIRSpec Analysis Tools, v0.3, Zenodo, doi:10.5281/zenodo.7299500  
 Brammer, G. 2023, grizli, v1.8.2, Zenodo, doi:10.5281/zenodo.7712834  
 Brammer, G. B., van Dokkum, P. G., & Coppi, P. 2008, *ApJ*, **686**, 1503  
 Calzetti, D. 2001, *PASP*, **113**, 1449  
 Capak, P. L., Carilli, C., Jones, G., et al. 2015, *Natur*, **522**, 455  
 Chabrier, G. 2003, *PASP*, **115**, 763  
 Chisholm, J., Tremonti, C. A., Leitherer, C., et al. 2015, *ApJ*, **811**, 149  
 Cleri, N. J., Trump, J. R., Backhaus, B. E., et al. 2022, *ApJ*, **929**, 3  
 Conroy, C., Gunn, J. E., & White, M. 2009, *ApJ*, **699**, 486  
 de Graaff, A., Rix, H.-W., Carniani, S., et al. 2023, arXiv:2308.09742  
 Dong, X., Wang, T., Wang, J., et al. 2008, *MNRAS*, **383**, 581  
 Dopita, M. A., & Sutherland, R. S. 1995, *ApJ*, **455**, 468  
 Draine, B. T., Dale, D. A., Bendo, G., et al. 2007, *ApJ*, **663**, 866  
 Eilers, A.-C., Simcoe, R. A., Yue, M., et al. 2023, *ApJ*, **950**, 68  
 Fan, X., Banados, E., & Simcoe, R. A. 2023, *ARA&A*, **61**, 373  
 Fan, X., Narayanan, V. K., Lupton, R. H., et al. 2001, *AJ*, **122**, 2833  
 Ferland, G. J., & Netzer, H. 1983, *ApJ*, **264**, 105  
 Fujimoto, S., Bezanson, R., Labbe, I., et al. 2023a, arXiv:2309.07834  
 Fujimoto, S., Kohno, K., Ouchi, M., et al. 2023b, arXiv:2303.01658  
 Fujimoto, S., Wang, B., Weaver, J., et al. 2023c, arXiv:2308.11609  
 Furtak, L. J., Labbé, I., Zitrin, A., et al. 2023a, arXiv:2308.05735  
 Furtak, L. J., Zitrin, A., Weaver, J. R., et al. 2023b, *MNRAS*, **523**, 4568  
 Glikman, E., Helfand, D. J., & White, R. L. 2006, *ApJ*, **640**, 579  
 Gordon, K. D., Clayton, G. C., Misselt, K. A., Landolt, A. U., & Wolff, M. J. 2003, *ApJ*, **594**, 279  
 Goulding, A. D., Greene, J. E., Setton, D. J., et al. 2023, *ApJL*, **955**, L24  
 Greene, J. E., & Ho, L. C. 2005, *ApJ*, **630**, 122  
 Greene, J. E., Labbe, I., Goulding, A. D., et al. 2023, arXiv:2309.05714  
 Greene, J. E., Seth, A., Kim, M., et al. 2016, *ApJL*, **826**, L32  
 Haiman, Z., & Loeb, A. 2001, *ApJ*, **552**, 459  
 Harikane, Y., Zhang, Y., Nakajima, K., et al. 2023, arXiv:2303.11946  
 Hogarth, L., Amorín, R., Vilchez, J. M., et al. 2020, *MNRAS*, **494**, 3541  
 Hopkins, P. F., Strauss, M. A., Hall, P. B., et al. 2004, *AJ*, **128**, 1112  
 Horne, K. 1986, *PASP*, **98**, 609  
 Inayoshi, K., Visbal, E., & Haiman, Z. 2020, *ARA&A*, **58**, 27  
 Isobe, Y., Ouchi, M., Nakajima, K., et al. 2023, *ApJ*, **956**, 139  
 Jeon, M., Pawlik, A. H., Greif, T. H., et al. 2012, *ApJ*, **754**, 34  
 Kashikawa, N., Ishizaki, Y., Willott, C. J., et al. 2015, *ApJ*, **798**, 28  
 Kaspi, S., Smith, P. S., Netzer, H., et al. 2000, *ApJ*, **533**, 631  
 Katz, H., Saxena, A., Cameron, A. J., et al. 2023, *MNRAS*, **518**, 592  
 Kocevski, D. D., Onoue, M., Inayoshi, K., et al. 2023, *ApJL*, **945**, L4  
 Kokorev, V., Jin, S., Magdis, G. E., et al. 2023, *ApJL*, **945**, L25  
 Kollmeier, J. A., Onken, C. A., Kochanek, C. S., et al. 2006, *ApJ*, **648**, 128  
 Koski, A. T., & Osterbrock, D. E. 1976, *ApJL*, **203**, L49  
 Labbé, I., Greene, J. E., Bezanson, R., et al. 2023a, arXiv:2306.07320  
 Labbé, I., Oesch, P. A., Bouwens, R. J., et al. 2013, *ApJL*, **777**, L19  
 Labbé, I., van Dokkum, P., Nelson, E., et al. 2023b, *Natur*, **616**, 266  
 Larson, R. L., Finkelstein, S. L., Kocevski, D. D., et al. 2023, *ApJL*, **953**, L29  
 Loeb, A., & Rasio, F. A. 1994, *ApJ*, **432**, 52

- Madau, P., & Rees, M. J. 2001, *ApJL*, **551**, L27
- Maiolino, R., Scholtz, J., Curtis-Lake, E., et al. 2023a, arXiv:2308.01230
- Maiolino, R., Scholtz, J., Witsstok, J., et al. 2023b, arXiv:2305.12492
- Massonnet, W., Volonteri, M., Dubois, Y., & Beckmann, R. S. 2023, *A&A*, **670**, A180
- Matsuoka, Y., Onoue, M., Kashikawa, N., et al. 2019, *ApJL*, **872**, L2
- Matsuoka, Y., Strauss, M. A., Kashikawa, N., et al. 2018, *ApJ*, **869**, 150
- Matthee, J., Naidu, R. P., Brammer, G., et al. 2023, arXiv:2306.05448
- Nagao, T., Murayama, T., & Taniguchi, Y. 2001, *ApJ*, **546**, 744
- Natarajan, P. 2011, *BASI*, **39**, 145
- Natarajan, P., Pacucci, F., Ferrara, A., et al. 2017, *ApJ*, **838**, 117
- Natarajan, P., Pacucci, F., Ricarte, A., et al. 2023, arXiv:2308.02654
- Neukova, M., Sirocky, M. M., Ivezić, Ž., & Elitzur, M. 2008a, *ApJ*, **685**, 147
- Neukova, M., Sirocky, M. M., Nikutta, R., Ivezić, Ž., & Elitzur, M. 2008b, *ApJ*, **685**, 160
- Nicholls, D. C., Kewley, L. J., & Sutherland, R. S. 2020, *PASP*, **132**, 033001
- Oke, J. B. 1974, *ApJS*, **27**, 21
- Omukai, K., Schneider, R., & Haiman, Z. 2008, *ApJ*, **686**, 801
- Osterbrock, D. E. 1978, *PhyS*, **17**, 285
- Osterbrock, D. E. 1989, *Astrophysics of Gaseous Nebulae and Active Galactic Nuclei* (Mill Valley: Univ. Science Books)
- Pacucci, F., Nguyen, B., Camiani, S., Maiolino, R., & Fan, X. 2023, arXiv:2308.12331
- Peng, C. Y., Ho, L. C., Impey, C. D., & Rix, H.-W. 2002, *AJ*, **124**, 266
- Peng, C. Y., Ho, L. C., Impey, C. D., & Rix, H.-W. 2010, *AJ*, **139**, 2097
- Reddy, N. A., Kriek, M., Shapley, A. E., et al. 2015, *ApJ*, **806**, 259
- Reddy, N. A., Oesch, P. A., Bouwens, R. J., et al. 2018, *ApJ*, **853**, 56
- Rees, M. J. 1984, *ARA&A*, **22**, 471
- Reines, A. E., & Volonteri, M. 2015, *ApJ*, **813**, 82
- Richards, G. T., Strauss, M. A., Fan, X., et al. 2006, *AJ*, **131**, 2766
- Rigby, J., Perrin, M., McElwain, M., et al. 2023, *PASP*, **135**, 048001
- Schleicher, D. R. G., Reinoso, B., Latif, M., et al. 2022, *MNRAS*, **512**, 6192
- Stern, J., & Laor, A. 2012, *MNRAS*, **423**, 600
- Stone, M. A., Lyu, J., Rieke, G. H., & Alberts, S. 2023, *ApJ*, **953**, 180
- Storey, P. J., & Zeippen, C. J. 2000, *MNRAS*, **312**, 813
- Übler, H., Maiolino, R., Curtis-Lake, E., et al. 2023, *A&A*, **677**, A145
- Vanden Berk, D. E., Richards, G. T., Bauer, A., et al. 2001, *AJ*, **122**, 549
- Wang, B., Fujimoto, S., Labbe, I., et al. 2023, arXiv:2308.03745
- Wang, L., Gao, F., Best, P. N., et al. 2021, *A&A*, **648**, A8
- Weaver, J. R., Cutler, S. E., Pan, R., et al. 2023, arXiv:2301.02671
- Yang, G., Caputi, K. I., Papovich, C., et al. 2023, *ApJL*, **950**, L5